



**Single Crystal Synthesis and Properties of the Two-Dimensional van der Waals Frustrated Magnets,  $Mn_2In_2Se_5$  and  $Mn_2Ga_2S_5$**

Journal:	<i>Journal of Materials Chemistry C</i>
Manuscript ID	TC-ART-09-2023-003550.R1
Article Type:	Paper
Date Submitted by the Author:	30-Nov-2023
Complete List of Authors:	Williams, Archibald; The Ohio State University, Chemistry and Biochemistry Reifsnyder, Alexander; The Ohio State University College of Engineering, Material Science and Engineering Yu, Bowen; The Ohio State University College of Engineering, Material Science and Engineering Moore, Curtis; The Ohio State University, Chemistry and Biochemistry Susner, Michael; Air Force Research Laboratory, Materials and Manufacturing Directorate RXEPE, Photonics Branch Windl, Wolfgang; The Ohio State University College of Engineering, Materials Science and Engineering McComb, David; The Ohio State University College of Engineering, Material Science and Engineering Goldberger, Joshua; The Ohio State University, Chemistry and Biochemistry

## ARTICLE

## Single Crystal Synthesis and Properties of the Two-Dimensional van der Waals Frustrated Magnets, $\text{Mn}_2\text{In}_2\text{Se}_5$ and $\text{Mn}_2\text{Ga}_2\text{S}_5$

Archibald J. Williams,<sup>a</sup> Alexander Reifsnnyder,<sup>b,c</sup> Bowen Yu,<sup>d</sup> Curtis E. Moore,<sup>a</sup> Michael A. Susner,<sup>e</sup> Wolfgang Windl,<sup>d</sup> David W. McComb,<sup>b,c</sup> and Joshua E. Goldberger<sup>a\*</sup>

Received 00th January 20xx,  
Accepted 00th January 20xx

DOI: 10.1039/x0xx00000x

There has been considerable interest in the search and design of two-dimensional (2D) van der Waals (vdW) compounds with exotic magnetic behavior. Here we establish the growth of phase pure crystals of  $\text{Mn}_2\text{In}_2\text{Se}_5$  and  $\text{Mn}_2\text{Ga}_2\text{S}_5$  and evaluate their structural, physical, and magnetic properties. These 2D vdW phases consist of double-octahedral thick  $\text{Mn}(\text{S}/\text{Se})_6$  layers capped by  $\text{InSe}_4$  or  $\text{GaS}_4$  tetrahedra. Transmission electron microscopy confirms phase purity with the absence of impurity intergrowths of other closely related 2D vdW phases including  $\text{Mn}(\text{In}/\text{Ga})_2(\text{Se}/\text{S})_4$  or  $\text{In}_4\text{Se}_3$ . Optical absorption measurements indicate these compounds to have indirect band gaps of 1.33 and 1.58 eV, respectively. We also establish the Raman signatures for both compounds.  $\text{Mn}_2\text{In}_2\text{Se}_5$  and  $\text{Mn}_2\text{Ga}_2\text{S}_5$  are significantly frustrated magnetic materials due to the competing magnetic interactions in this double-thick triangular arrangement of metal atoms. They have magnetic transition temperatures of 7 and 13K, respectively, compared to Weiss constants of -198 and -340 K, respectively. AC susceptibility experiments indicate that both  $\text{Mn}_2\text{In}_2\text{Se}_5$  and  $\text{Mn}_2\text{Ga}_2\text{S}_5$  exhibit significant spin glass character. The significant magnetic frustration makes these materials unique 2D magnetic vdW building blocks.

### Introduction

Since the discovery of single-layer thick ferromagnetism in  $\text{CrI}_3$  in 2017<sup>1</sup> there has been an expansion in the number of known 2D van der Waals (vdW) magnetic materials<sup>2</sup>. The discovery of 2D magnetism has opened avenues to investigate many exotic magnetic analogues to properties that are observed in non-magnetic systems such as Moiré superlattices<sup>3-8</sup> as well as in vertical heterostructures of different vdW materials<sup>9-11</sup>. Additionally, these magnetic vdW materials allow for the exploration of new types of spintronic devices<sup>12-15</sup>. However, the development of these devices has been hindered by the incredible air sensitivity of many of these materials both in the bulk and upon exfoliation, most notably in the transition metal trihalides  $\text{MX}_3$  (M = transition metal, X = Cl, Br, I)<sup>16-19</sup>.

Multiple avenues have been explored to design materials that are more robust to ambient conditions including capping with air stable hBN layers and using air stable transition metal dichalcogenides as hosts for magnetic doping<sup>20-25</sup>. Additionally,

recent work has led to the identification of 2D vdW compounds that are inherently more resilient towards oxidation including  $\text{CrSBr}$ <sup>26-28</sup> and the  $\text{MPC}_3$  (Ch = S, Se, Te) family<sup>29, 30</sup>. Most of these systems are ordered magnetic systems with either ferromagnetic or antiferromagnetic long-range ordering and minimal degrees of magnetic frustration. Magnetic frustration occurs when the magnetic coupling interactions between all neighbouring spins cannot be satisfied simultaneously, leading to a disordered glassy magnetic ground state and/or greatly suppressed magnetic transition temperatures. Numerous geometrical patterns of magnetic elements are known to lead to this frustration, such as triangular<sup>31-34</sup> and Kagome lattices<sup>35, 36</sup>. These disordered phases have attracted considerable interest in the materials community, both in spin-dynamic devices and in quantum spin liquids whereby this frustration inhibits ordering at any temperature<sup>37, 38</sup>.

By far the most well-studied 2D vdW materials are the transition metal dichalcogenides of stoichiometry  $\text{MCh}_2$ . These materials have structures that consist of layers of  $\text{MCh}_6$  edge sharing octahedra in a triangular lattice that are held together by vdW forces. These phases generally form for many early and late transition metals, but not for the most magnetic 1<sup>st</sup> row elements (Mn, Fe, Co, Ni) which instead crystallize into pyrite or other 3D structures<sup>39</sup>. However, many magnetic transition metals crystallize into the  $\text{ZnIn}_2\text{Se}_4$  2D vdW structure-type, in which each layer features this triangular edge-sharing octahedral motif but is capped on the top and bottom faces by corner sharing metal-chalcogen tetrahedra. These compounds have a nominal composition of  $\text{MTr}_2\text{Ch}_4$  where M is a divalent transition metal (M = Mn, Fe, Ni, Zn), Tr is a trivalent triel atom (Tr = Al, Ga, In) and Ch is a chalcogen (S, Se). Multiple  $\text{MTr}_2\text{Ch}_4$

<sup>a</sup> Department of Chemistry and Biochemistry, The Ohio State University, 100 W. 18th Avenue, Columbus, Ohio 43210, United States

<sup>b</sup> Department of Materials Science and Engineering, The Ohio State University, Fontana Laboratories, 2136, 140 W 19th Ave, Columbus, OH 43210, USA

<sup>c</sup> Center for Electron Microscopy and Analysis, The Ohio State University, 1305 Kinnear Rd, Columbus, OH 43212, USA.

<sup>d</sup> Department of Materials Science and Engineering, The Ohio State University, Columbus, Ohio 43210, United States

<sup>e</sup> The Air Force Research Laboratory, Materials and Manufacturing Directorate RXEPE, Photonics Branch 2179 12th Street, Wright-Patterson AFB, OH 45433

Electronic Supplementary Information (ESI) available: [details of any supplementary information available should be included here]. See DOI: 10.1039/x0xx00000x

stacking polytypes are known including 1-layer Trigonal (1T), 2-layer hexagonal (2H) and 3-layer Rhombohedral (3R) structures<sup>40</sup>. Previous studies have shown that these compounds are generally semiconducting<sup>41</sup> where the energy gap is dependent on the transition metal. For example, FeGa<sub>2</sub>S<sub>4</sub> is a narrow gap semiconductor of 0.11 eV<sup>42</sup> while the gap in MnIn<sub>2</sub>Se<sub>4</sub> is 1.43 eV<sup>43</sup>. The M=Mn, Fe, and Ni derivatives have significant magnetic frustration indices (*f*), a term defined as the ratio of the Weiss constant ( $\theta_w$ ) from the Curie-Weiss plot to the observed magnetic transition temperature ( $T_N$ ). FeGa<sub>2</sub>S<sub>4</sub> and NiGa<sub>2</sub>S<sub>4</sub> have *f*>10, which is attributed to the triangular network of the transition metals in these layers<sup>44</sup>. Additionally, the capping TrCh<sub>4</sub> tetrahedra make these 2D van der Waals compounds air and water stable.

During the syntheses of these MTr<sub>2</sub>Ch<sub>4</sub> compounds, impurities of a closely related phase with stoichiometry M<sub>2</sub>Tr<sub>2</sub>Ch<sub>5</sub> were found<sup>45-47</sup>. These compounds are similar but have a double-octahedra thick layers of the edge-sharing MCh<sub>6</sub> framework. This second MCh<sub>6</sub> layer is most often in an edge sharing configuration with the layer below and can be thought of as a double octahedral thick [111] slice of a MCh rock salt lattice. Phase-pure forms of these materials have not been established for most of these compounds. Thus, very little is known about the properties of most of these materials. One notable exception is Fe<sub>2</sub>Ga<sub>2</sub>S<sub>5</sub> having been synthesized phase pure previously and being characterized as a narrow gap semiconductor (5 meV) through transport measurements and exhibiting long range antiferromagnetic order at 110K in contrast to the MTr<sub>2</sub>Ch<sub>4</sub> compounds<sup>42, 44</sup>. The much higher transition temperature in this material is attributed to the strong 180° superexchange coupling that arises between Fe sites in one layer to Fe sites in the second layer. Also, during the preparation of this manuscript, the synthesis and magnetic properties of phase pure crystals of Mn<sub>2</sub>Ga<sub>2</sub>S<sub>5</sub> was reported<sup>48</sup>, showing this phase to be a highly frustrated magnetic system, although the experimental characterization of its structural and optical properties has yet to be fully established.

Here, we establish a chemical vapor transport (CVT) route for the preparation of phase pure Mn<sub>2</sub>In<sub>2</sub>Se<sub>5</sub> and Mn<sub>2</sub>Ga<sub>2</sub>S<sub>5</sub> powders and crystals, allowing for the characterization of the structural, electronic, and magnetic properties. Both powder and single crystal diffraction as well as transmission electron microscopy indicate these materials to be phase pure. Diffuse reflectance absorption measurements show both materials to be indirect gapped semiconductors with band gaps of 1.33 eV and 1.58 eV for Mn<sub>2</sub>In<sub>2</sub>Se<sub>5</sub>, and Mn<sub>2</sub>Ga<sub>2</sub>S<sub>5</sub>, respectively. We characterize the Raman spectra of both compounds, as it is one of the most prevalent techniques for identifying the structure, stacking sequence and layer thicknesses of layered 2D materials. These compounds exhibit a high degree of magnetic frustration with spin glass freezing transition temperatures of 7 and 13.6 K, for Mn<sub>2</sub>In<sub>2</sub>Se<sub>5</sub> and Mn<sub>2</sub>Ga<sub>2</sub>S<sub>5</sub>, respectively, which is far smaller than their respective Weiss constants of -190 K, and -340 K. The spin-glass behaviour is relatively rare among 2D van der Waals magnets, making these air and water stable compounds ripe for future exploration of exotic spin behaviour.

## Experimental

### Synthesis of Mn<sub>2</sub>In<sub>2</sub>Se<sub>5</sub>

Phase pure powders of Mn<sub>2</sub>In<sub>2</sub>Se<sub>5</sub> were synthesized by a two-step process. In the first step, stoichiometric amounts of Mn powder (99.95%, Alfa Aesar, typically 0.2788 g), In shot (99.9%, Aldrich, typically 0.5970 g) and Se powder (99.999%, Alfa Aesar, typically 1.0056 g) were added to a quartz ampoule and sealed under <70 mTorr. These elements were stored and loaded into the quartz ampoule under an inert Ar atmosphere to minimize any surface oxide. To prevent the reaction of elemental Mn with quartz, this reaction was done in quartz tubes that had been carbon coated by graphitizing the inside of the tube with isopropyl alcohol. This tube was added to a muffle furnace, ramped up to 1050 °C over 8 hr to minimize rapid Se over pressurization of the tube, heated at 1050 °C for 48 hours, cooled to 750 °C at 2 °C/hr, before cooling to room temperature over 6 hours. The resulting ingot had majority Mn<sub>2</sub>In<sub>2</sub>Se<sub>5</sub> flakes with impurity MnIn<sub>2</sub>Se<sub>4</sub> and In<sub>4</sub>Se<sub>3</sub> phases. Phase pure Mn<sub>2</sub>In<sub>2</sub>Se<sub>5</sub> flakes could not be isolated from the ingot without performing a second step. This ingot was ground and used as precursors for the growth of Mn<sub>2</sub>In<sub>2</sub>Se<sub>5</sub> (usually 1.2938 g) crystals via chemical vapor transport using I<sub>2</sub> (usually 0.0485 g) across a temperature gradient from 780 °C to 720 °C for 4 days in a quartz ampoule of 18 cm in length and 1.5 cm inner diameter, after which crystals having 2-5 mm length and width, and 100- 500 μm thickness were observed. After synthesis, Mn<sub>2</sub>In<sub>2</sub>Se<sub>5</sub> was found to be air-stable and handled in air.

### Synthesis of Mn<sub>2</sub>Ga<sub>2</sub>S<sub>5</sub>

Powders of Mn<sub>2</sub>Ga<sub>2</sub>S<sub>5</sub> were grown from a reaction of the binary components MnS and Ga<sub>2</sub>S<sub>3</sub>. MnS was prepared by the grinding together and pelletizing of stoichiometric amounts of Mn (99.95%, Alfa Aesar, normally 0.3162 g) and S (99.5% Mallinckrodt, recrystallized, normally 0.1842 g) in a glove box. This pellet was then added to an ampoule sealed at <70 mTorr under Ar. The tube was put in a muffle furnace and slowly heated up to 750 °C over 12 hours to minimize S over pressurization and reacted for 48 hours before the tube was quenched to room temperature using a sand bath. Ga<sub>2</sub>S<sub>3</sub> was synthesized by a high energy ball mill reaction in a stainless-steel milling jar with stainless steel balls using an MTI Corporation MSK-SFM-3 Desktop high speed vibrating ball mill. Stoichiometric amounts of Ga pellets (99.99999%, Alfa Aesar, typically 1.0356 g) and S (99.5% Mallinckrodt, recrystallized, typically 0.7143 g) were loaded in the milling jar in a glove box with a 20:1 ball to material ratio. This material was ball milled for 3 cycles of 30 minutes at 1200 RPM after which point the material was recovered, opening the container in an Ar-filled glove box. Powders of Mn<sub>2</sub>Ga<sub>2</sub>S<sub>5</sub> were obtained by reacting together stoichiometric amounts of MnS (usually 0.2970 g) and Ga<sub>2</sub>S<sub>3</sub> (usually 0.4062 g) via grinding in a mortar and pestle and sealing this mixture in a quartz ampoule. This ampoule was ramped to 950 °C over 8 hours and held at that temperature for 96 hours before cooling to room temperature over 8 hours

resulting in brick red  $\text{Mn}_2\text{Ga}_2\text{S}_5$ . Small single crystals of  $\text{Mn}_2\text{Ga}_2\text{S}_5$  having lengths and widths of 100  $\mu\text{m}$  were grown from presynthesized  $\text{Mn}_2\text{Ga}_2\text{S}_5$  powder (normally 0.5692 g) by CVT using  $\text{AlCl}_3$  (normally 0.0503g) transport agent under a temperature gradient from 900  $^\circ\text{C}$  and 840  $^\circ\text{C}$  for 12 days in a 19 cm long and 1.5 cm inner diameter quartz tube. After synthesis,  $\text{Mn}_2\text{Ga}_2\text{S}_5$  was found to be air-stable and handled in air.

### Structural Characterization

In air, grown crystals of  $\text{Mn}_2\text{In}_2\text{Se}_5$  were ground into a fine powder for powder X-ray diffraction characterization (PXRD). Both  $\text{Mn}_2\text{In}_2\text{Se}_5$  and  $\text{Mn}_2\text{Ga}_2\text{S}_5$  were analysed using a Bruker D8 Advance powder X-ray diffractometer using  $\text{Cu K}\alpha_1$  radiation that was generated at 40 kV and 40 mA. Powder X-ray diffraction patterns were used for structural confirmation and Rietveld refinement using TOPAS Commercial.

The single crystal X-ray diffraction studies on  $\text{Mn}_2\text{Ga}_2\text{S}_5$  were carried out on a Bruker Kappa Photon III CPAD diffractometer equipped with  $\text{Mo K}\alpha$  radiation ( $\lambda = 0.71073 \text{ \AA}$ ). A  $0.056 \times 0.044 \times 0.038 \text{ mm}$  piece of an orange plate was mounted on a Cryloop with Paratone 24EX oil. Data were collected in a nitrogen gas stream at 100(2) K using  $\phi$  and  $\omega$  scans. Crystal-to-detector distance was 40 mm and exposure time was 20 seconds per frame using a scan width of  $2.0^\circ$ . Data collection was 98.8% complete to  $25.00^\circ$  in  $\theta$  ( $0.83 \text{ \AA}$ ). A total of 4696 reflections were collected covering the indices,  $5 \leq h \leq 5$ ,  $5 \leq k \leq 5$ ,  $21 \leq l \leq 21$ . 268 reflections were found to be symmetry independent, with a  $R_{\text{int}}$  of 0.0560. Indexing and unit cell refinement indicated a primitive, trigonal lattice. The space group was found to be  $P\bar{3}m1$ . The data were integrated using the Bruker SAINT software program and scaled using the SADABS software program. Solution by direct methods (SHELXT) produced a complete phasing model for refinement.

### Electron Microscopy Characterization

Plan-view samples were prepared by ultrasonic exfoliation. Samples were exfoliated for 15 minutes in isopropanol then drop-cast onto lacey carbon-coated TEM grids. Cross-section samples were milled using a focused ion beam (FIB). FIB lamellae were prepared with a FEI Helios NanoLab 600 DualBeam. Lamellae were polished using low energy Ar ion milling using a Fischione Model 1040 Nanomill. STEM-HAADF images were collected with a probe-corrected Thermo Scientific Themis Z S/TEM operated at 300 kV with a screen current of  $\sim 60 \text{ pA}$  equipped with a Super-X energy dispersive x-ray (EDX) system.

### Magnetic Measurements

DC Magnetization measurements of both materials were measured using a Quantum Design MPMS3 superconducting quantum interference device (SQUID). Powders were set within an inverted gelatin capsule held together with Kapton tape. These pellets were added to a straw and aligned to position for

analysis. Measurements of the temperature dependent DC magnetic susceptibility ( $X$  vs.  $T$ ) were run by first cooling the sample to 2 K under no applied field in zero-field cooled (ZFC) plots, and measuring using a 500 Oe measurement field upon warming. Field cooled (FC) plots were performed after cooling in a 500 Oe cooling field and a 500 Oe measurement field. Measurements of Magnetization vs. Field ( $M$  vs.  $H$ ) plots were done by cooling to 2K under no applied field before sweeping the field from 0 to 4 T and then to  $-4 \text{ T}$  before this trace was ran in duplicate. AC Magnetization measurements were measured on the same samples using a Quantum Design Physical Property Measurement System (PPMS) using an ACMS option. Samples were measured using a 10 Oe AC measurement field across a range of frequencies.

### Optical Absorbance Measurements

Diffuse reflectance absorption (DRA) spectra were collected on powders of each material using a Perkin Elmer Lambda 950 UV/Vis Spectrometer from 250 to 2500 nm with dried  $\text{BaSO}_4$  as the background and diluent salt. This reflectance data was then converted into absorbance using the Kubelka-Munk function.

### Raman characterization

Raman scattering spectra were acquired using a Renishaw Raman IR microprobe with an inVia confocal Raman microscope, using a 785 nm light source, and a charge-coupled detector. A Pike Technologies KRS-5 polarizer was placed before the charge-coupled detector for the 785 nm light source and aligned to different polarization wavelengths to measure the polarization angle dependence of the Raman spectra. Nearly identical Raman spectra were observed using a 633 or 514 nm light source, as well as a Thorlabs  $2'' \times 2''$  film polarizing filter in place of the KRS-5 polarizer.

### DFT Methodology

Phonon dispersion relations and densities of states were determined through post-processing with Alfé's Phon package<sup>49</sup> of the Hessian matrix, calculated using the Vienna Ab-initio Simulation Package (VASP)<sup>50</sup> with the help of the small-displacement method with displacements of 0.01  $\text{Å}$  within  $3 \times 3 \times 1$  and  $5 \times 5 \times 1$  hexagonal supercells for  $\text{Mn}_2\text{In}_2\text{Se}_5$  and  $\text{Mn}_2\text{Ga}_2\text{S}_5$ , respectively. All calculations were performed with Projector Augmented Wave Perdew-Burke-Ernzerhof (PAW-PBE) potentials<sup>51</sup> and a kinetic-energy cutoff of 270 eV. Brillouin-zone sampling was performed with Methfessel-Paxton smearing<sup>52</sup> with a  $k$ -spacing of  $0.25 \text{ \AA}^{-1}$ . For both magnetic structures, Mn had antiferromagnetic ordering with spins alternating across the layers. The electronic correlations in Mn were accounted for by a Hubbard-U of 5 eV for the In and 2 eV for the Ga compound, applied within Dudarev's rotationally invariant formulation<sup>53</sup>. For the van-der-Waals interactions, Grimme's DFT-D2 model was used<sup>54</sup>. Due to the very sharp rhombohedral cell shape of  $\text{Mn}_2\text{In}_2\text{Se}_5$ , which caused major convergence problems, relaxation and phonon calculations

were performed using the hexagonal unit cell. The relaxed rhombohedral lattice parameters for  $\text{Mn}_2\text{In}_2\text{Se}_5$  were found to be 16.585 Å and 13.86° for the angle, while the hexagonal lattice parameters for  $\text{Mn}_2\text{Ga}_2\text{S}_5$  were  $a = 3.710$  Å and  $c = 15.188$  Å.

## Results and Discussion

### Crystal Growth and Structural Characterization

Significant efforts were devoted towards the synthesis of phase pure crystals of both  $\text{Mn}_2\text{In}_2\text{Se}_5$  and  $\text{Mn}_2\text{Ga}_2\text{S}_5$ .  $\text{Mn}_2\text{In}_2\text{Se}_5$  crystals were synthesized in a two-step reaction. First, high purity, >95% wt percent,  $\text{Mn}_2\text{In}_2\text{Se}_5$  is prepared from direct reaction and slow cooling of the elements with trace impurities of layered  $\text{In}_4\text{Se}_3$  and  $\text{MnIn}_2\text{Se}_4$ . A subsequent CVT crystal growth step with  $\text{I}_2$  resulted in large crystals with 2-5 mm lengths and widths, and thicknesses of ~50-500 μm (Figure 1b). Some of these crystals were ground for powder XRD confirming the 3R  $R\bar{3}m$  polytype and the absence of trace impurity reflections (Figure 1a, c). Phase pure powder of  $\text{Mn}_2\text{Ga}_2\text{S}_5$  having a 1T  $P\bar{3}m1$  polytype was synthesized through a solid-state reaction of the binary phase precursors  $\text{MnS}$  and  $\text{Ga}_2\text{S}_3$  and crystals of 150-300 μm length and width, with ~10 μm thickness were grown through CVT using  $\text{AlCl}_3$  as a transport agent (Figure 1d, e). No impurities were observed in the powder XRD pattern (Figure 1f). Both compounds crystallize into phases in which the middle  $\text{Mn}(\text{S}/\text{Se})_6$  layers can be thought of as being double-octahedral thick 111 slices of the rock salt lattice. Thus, each Mn has three interlayer  $\text{Mn}(\text{layer 1})-\text{S}(\text{Se})-\text{Mn}(\text{layer 2})$  bond angles that are 180 degrees, and three that are 90 degrees.

The structure of  $\text{Mn}_2\text{Ga}_2\text{S}_5$  across an entire crystal was confirmed by single crystal diffraction. The Mn and Ga Wyckoff sites had complete site ordering, in agreement with previous reports on this compound<sup>47,48</sup>. The crystal structure was further confirmed via Rietveld refinement of ground up powder. The pliability of the  $\text{Mn}_2\text{In}_2\text{Se}_5$  crystals hindered attempts to obtain a single crystal structure solution. Thus, the crystal structure of  $\text{Mn}_2\text{In}_2\text{Se}_5$  was determined using Rietveld analysis of the powders (Table S6, S7, Figure S2). In  $\text{Mn}_2\text{In}_2\text{Se}_5$ , a satisfactory fit could not be achieved when attempting to refine the octahedral and tetrahedral In positions with full Mn and In occupancy, respectively. Furthermore, doing so resulted in negative  $B_{\text{eq}}$  values for the Mn site and much larger positive values for the In site. Considering that  $\text{Mn}^{2+}$  and  $\text{In}^{3+}$  have very similar Shannon ionic radii in both tetrahedra and octahedra geometries (within 0.04 Å), we refined the partial occupancies of both sites to allow In to mix onto the Mn position and vice versa. A much better fit was achieved with ~21% site mixing between the Mn and In sites. This site mixing is in agreement with the initially reported structural solution.

We also performed high-angle annular dark-field scanning transmission electron microscopy (HAADF-STEM) of both compounds to confirm the atomic structure, single crystallinity, and absence of intergrowth impurities. HAADF-STEM imaging confirmed the structure of  $\text{Mn}_2\text{In}_2\text{Se}_5$  through both cross sectional (Figure 2a) and plan-view imaging (Figure 2b). The 9-

atom thick  $\text{Mn}_2\text{In}_2\text{Se}_5$  sequence is readily apparent when imaging down the (100) plane. The much more strongly scattering In atoms are localized on the tetrahedral sites at the top and bottom of each 9-atom thick layer. The 9-atom thick 1T van der Waals layer of  $\text{Mn}_2\text{Ga}_2\text{S}_5$  was also confirmed via cross sectional imaging. Both materials show excellent crystallinity over a large area and a notable absence of 7-atom thick

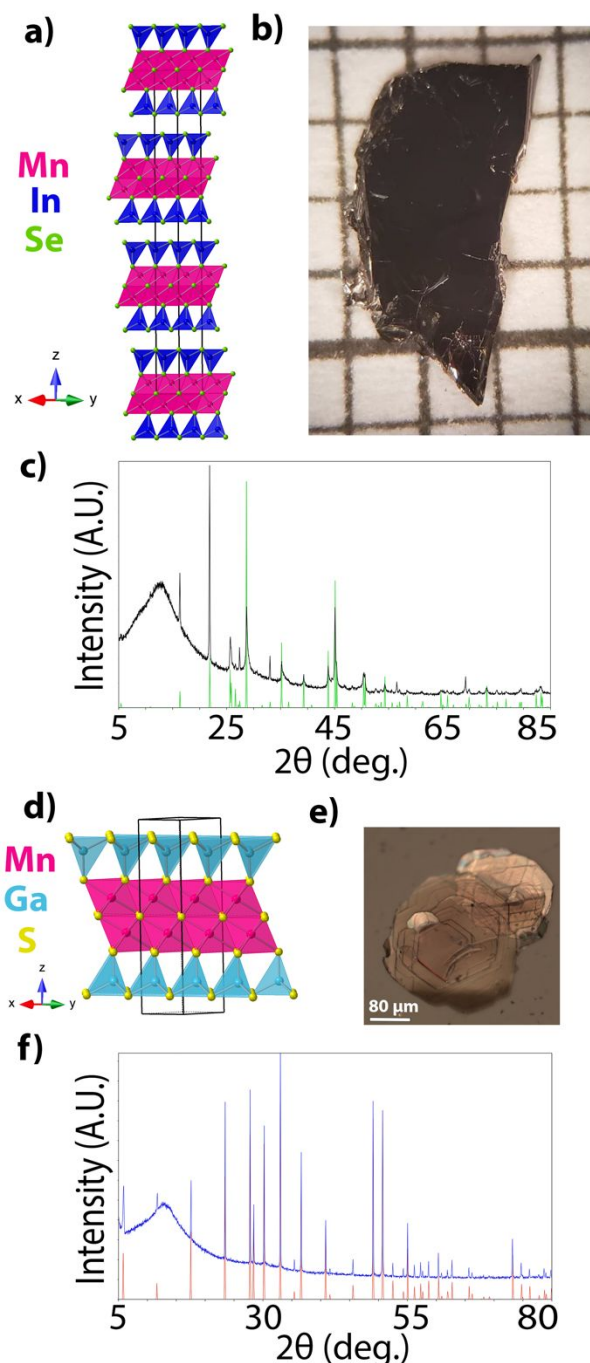


**Fig. 1.** Crystal structure of (a) 3R  $\text{Mn}_2\text{In}_2\text{Se}_5$  and (d) 1T  $\text{Mn}_2\text{Ga}_2\text{S}_5$  viewed from the [110] direction. As grown single crystals of (b)  $\text{Mn}_2\text{In}_2\text{Se}_5$  on mm-grid paper and (e)  $\text{Mn}_2\text{Ga}_2\text{S}_5$  with scale bar inset. Powder X-ray Diffraction (PXRD) showing phase purity of the grown material for (c)  $\text{Mn}_2\text{In}_2\text{Se}_5$  and (f)  $\text{Mn}_2\text{Ga}_2\text{S}_5$ , with the calculated structures shown in green and red, respectively. The broad hump at ~15° 2θ is a background signal from the sample holder.

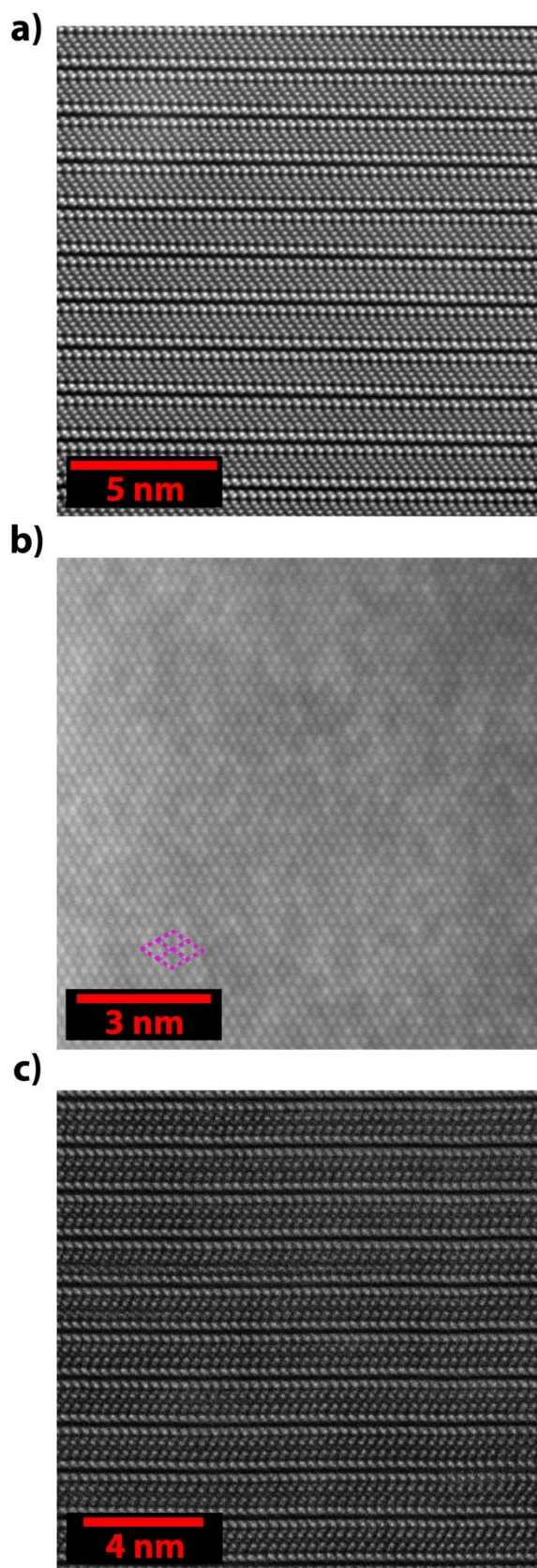


**Fig. 2.** HAADF-STEM images of (a)  $\text{Mn}_2\text{In}_2\text{Se}_5$  viewed along the [100] direction, (b)  $\text{Mn}_2\text{In}_2\text{Se}_5$  as viewed along the [001] direction, and (c)  $\text{Mn}_2\text{Ga}_2\text{S}_5$  viewed along the [100] direction. In b the hexagonal unit cell is inscribed in purple.

$\text{MnIn}_2\text{Se}_4/\text{MnGa}_2\text{S}_4$  or  $\text{In}_4\text{Se}_3$  layers across the entire cross-sections (Figure S3). In contrast, HAADF-STEM imaging on isolated  $\text{Mn}_2\text{In}_2\text{Se}_5$  flakes grown from the slow cool synthesis without the CVT purification step exhibited intergrowths of 7-atom thick  $\text{MnIn}_2\text{Se}_4$  layers (Figure S4).

#### Optical Absorption

The optical absorption of these materials was investigated through diffuse reflectance absorption on powder samples. The reflectance data were converted into a Kubelka-Munk function and then plotted using the conventional Tauc-Davis-Mott expression for 3D materials to assess the nature of the direct and indirect gaps seen in these materials. Both materials (Figure 4a, b) demonstrate indirect band gap semiconductor behavior with gaps of 1.33 eV in  $\text{Mn}_2\text{In}_2\text{Se}_5$  and 1.58 eV in  $\text{Mn}_2\text{Ga}_2\text{S}_5$ . The direct gaps are much higher in energy and estimated to be 1.77 eV for  $\text{Mn}_2\text{In}_2\text{Se}_5$  and 1.92 eV for  $\text{Mn}_2\text{Ga}_2\text{S}_5$ . Confirming this, powders of  $\text{Mn}_2\text{In}_2\text{Se}_5$  are black, indicative of absorption across the visible spectrum while powders of  $\text{Mn}_2\text{Ga}_2\text{S}_5$  have a brick red color indicative of an absorption onset close to the long wavelength edge of the visible spectrum. No fluorescence was observed in either sample upon excitation with 365 nm light, further indicative of an indirect band gap material.

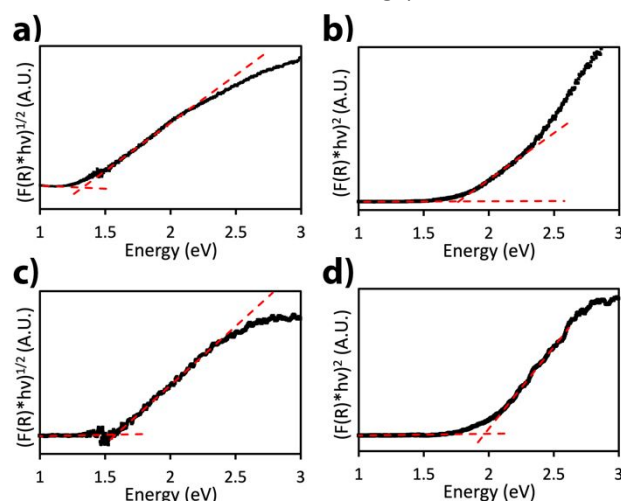


**Fig. 3.** Diffuse reflectance absorbance spectra of (a,b)  $\text{Mn}_2\text{In}_2\text{Se}_5$  and (c,d)  $\text{Mn}_2\text{Ga}_2\text{S}_5$ , fitted using the Tauc-Davis-Mott expressions for (a, c) a 3D indirect allowed and (b, d) a 3D direct allowed transition.

#### Raman spectroscopy

Raman spectroscopy is one of the most powerful methods of characterizing 2D materials both in the bulk and upon exfoliation to few layers. Therefore, we evaluated the Raman spectra of both compounds in single crystal form using 785 nm (1.58 eV) coherent light, which is above the band gap of both materials. Assuming perfect site ordering, both compounds would be expected to have 8 Raman active modes.  $\text{Mn}_2\text{In}_2\text{Se}_5$ , which has the  $R\bar{3}m$  space group, has 4 atoms on different  $6c$  Wyckoff sites (0 0 z), and a Se atom on the  $3a$  Wyckoff site (0 0 0). Each atom on the  $6c$  site will have 1  $A_{1g}$  and 1  $E_g$  vibration, while the atom on the  $3a$  site is Raman inactive.  $\text{Mn}_2\text{Ga}_2\text{S}_5$ , which crystallizes into the  $P\bar{3}m1$  space group, has 4 atoms on the  $2d$  site ( $1/3$   $2/3$  z), and a S atom on the  $1b$  site (0 0  $1/2$ ). Each

atom on the  $2d$  site will have 1  $A_{1g}$  and 1  $E_g$  vibration, while the atom on the  $1b$  site is Raman inactive. Thus, both compounds are expected to have 4  $A_{1g}$  modes and 4  $E_g$  Raman active modes. The Raman spectra of  $Mn_2In_2Se_5$  and  $Mn_2Ga_2S_5$  are shown in Figure 4a and 4b, respectively. Experimentally we can identify 5 Raman active modes in both  $Mn_2In_2Se_5$  and  $Mn_2Ga_2S_5$  at energies greater than  $90\text{ cm}^{-1}$ , the resolution of our instrument. As expected, the modes in  $Mn_2In_2Se_5$  are shifted to lower energies from that of  $Mn_2Ga_2S_5$  considering the much larger mass of In and Se, relative to Ga and S. The Raman modes seen in  $Mn_2In_2Se_5$  are also much broader than in  $Mn_2Ga_2S_5$ , which is consistent with the presence of Mn/In site disorder.

First principles calculations were performed to facilitate the assignment of the symmetry of these modes as either  $E_g$  or  $A_{1g}$  (Figure 4c-h). For  $Mn_2In_2Se_5$ , in order to model the site disorder, a  $3 \times 3 \times 1$  supercell was used in which 20% of the Mn and In sites were swapped. First-order Raman modes will only appear for the  $\Gamma$  point phonon modes with gerade symmetry. In  $Mn_2In_2Se_5$ , the modes centred around 180 and  $163\text{ cm}^{-1}$  had  $E_g$  symmetry while the modes at 270, 200,  $160\text{ cm}^{-1}$  were  $A_{1g}$  modes (Figure 4c). All other  $A_{1g}$  and  $E_g$  modes are calculated to occur below  $90\text{ cm}^{-1}$ . These are relatively close to the Raman modes observed in the experimental spectrum, which occur at

260, 195, 171, 160 and  $137\text{ cm}^{-1}$ . However, the experimental Raman spectrum has an additional mode at  $225\text{ cm}^{-1}$  which is relatively close in energy to the  $240\text{ cm}^{-1}$  peak in the phonon density of states (Figure 4d). It is possible that this vibration is due to disorder lifting the selection rules or corresponds to a higher-order Raman mode, but further work is needed to conclusively determine the origin of this peak<sup>55</sup>. In  $Mn_2Ga_2S_5$  the modes at 306 and  $215\text{ cm}^{-1}$  were calculated to have  $E_g$  symmetry while the modes at 421, 297, and  $208\text{ cm}^{-1}$  have  $A_{1g}$  symmetry. All other  $A_{1g}$  and  $E_g$  modes are calculated to be below  $90\text{ cm}^{-1}$  and are thus outside the energy range of our instrument. These are relatively close in energy to the measured Raman modes at 432, 306, 291, 213 and  $203\text{ cm}^{-1}$ . Two additional Raman modes are detected at 340 and  $380\text{ cm}^{-1}$  in all  $Mn_2Ga_2S_5$  crystals, these are again relatively close to energies where a distinct peaks in the phonon density of states occurs (Fig. 4g). Similarly, it is possible that these vibrations correspond to higher-order Raman modes or result from intrinsic defects, but conclusive confirmation requires a more detailed study that is beyond the scope of this work.

### Magnetic Measurements

The magnetic properties of both materials were investigated through SQUID magnetometry for DC magnetization and a PPMS using ACMS mode for AC magnetization. Figure 5 a and b show the DC magnetization versus temperature plots for  $Mn_2In_2Se_5$  and  $Mn_2Ga_2S_5$ , while the insets show the Curie-Weiss fitting of the inverse susceptibility. Both materials exhibit typical Curie-Weiss behavior above 50K with strong antiferromagnetic short-range coupling as demonstrated by the highly negative Weiss constants ( $\theta_w$ ) of -198 K and -340 K for  $Mn_2In_2Se_5$  and  $Mn_2Ga_2S_5$ , respectively. Despite this strong short-range coupling, both materials undergo low temperature transitions of 7 K for  $Mn_2In_2Se_5$  and 14 K for  $Mn_2Ga_2S_5$ . From the Curie-Weiss fitting, the Curie constant yields local magnetic moments of  $6.0\ \mu_B$  per Mn atom in  $Mn_2In_2Se_5$  and  $6.4\ \mu_B$  per Mn atom in  $Mn_2Ga_2S_5$ , similar to the  $5.92\ \mu_B$  per atom expected for 5 unpaired spins, suggesting  $Mn^{2+} d^5$  high-spin magnetic sites. Magnetization vs. applied field measurements (Figure 5c,d) for powders at 2 K confirm that this transition is generally antiferromagnetic in nature showing both low magnetization per Mn atom and a linear response to field. Despite a linear trend,  $Mn_2In_2Se_5$  shows a weak ferromagnetic signature at low field not seen in  $Mn_2Ga_2S_5$ . This is demonstrated in the partial cusp seen in the magnetization vs temperature (Figure 5a) and both the deviation from linearity and greater magnitude in the magnetization vs. applied field (Figure 5c). This weak ferromagnetic response likely arises from distortion of the antiferromagnetic order by the site disorder of Mn and In atoms in the lattice which is present in  $Mn_2In_2Se_5$ , but not in  $Mn_2Ga_2S_5$ .

Despite the evidence for an overall antiferromagnetic description of the magnetic ordering in these materials, there is a high degree of magnetic frustration. The frustration index for both compounds is greater than 20, suggesting significant magnetic complexity. AC susceptibility vs temperature

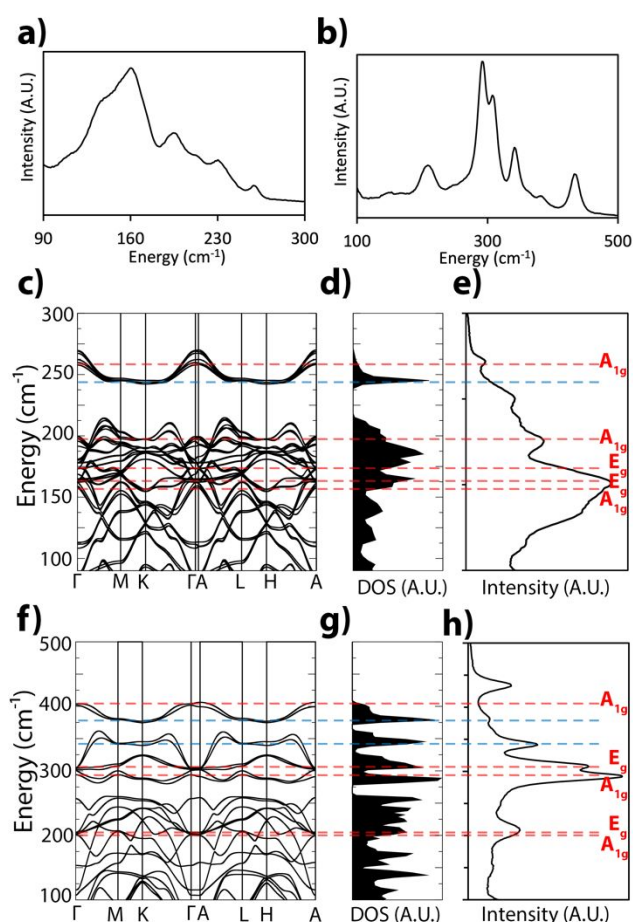


**Fig. 4.** Raman spectrum of (a)  $Mn_2In_2Se_5$  and (b)  $Mn_2Ga_2S_5$ . Calculated phonon band structure (c), density of states (d) and match to experiment (e) for  $Mn_2In_2Se_5$ . Calculated phonon band structure (f), density of states (g) and match to experiment (h) for  $Mn_2Ga_2S_5$ . Red lines show matches to calculated phonons at  $\Gamma$  and blue lines show matches to phonons at other points in the Brillouin zone.

measurements were run to confirm if this transition can be better described as an ordered antiferromagnet or a spin glass system. Figure 5e and 5f show that upon varying the frequency of a 10 Oe applied AC measurement field from 400 to 10000 Hz, where the cusp of magnetization clearly shifts to higher temperature at higher frequency in both materials. The  $\text{Mn}_2\text{Ga}_2\text{S}_5$  AC susceptibility shows a classical spin glass peak, while in  $\text{Mn}_2\text{In}_2\text{Se}_5$  the peak has less of a drop off at lower temperatures, due to the residual magnetic contributions caused by the site disorder.

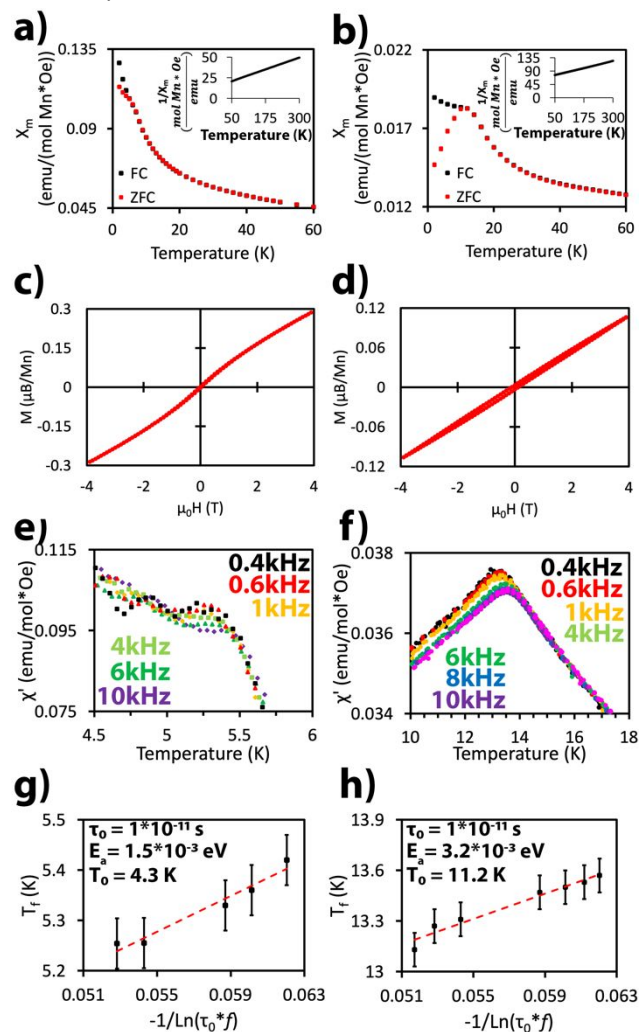


**Fig. 5.** Magnetic susceptibility versus temperature plots of (a)  $\text{Mn}_2\text{In}_2\text{Se}_5$  and (b)  $\text{Mn}_2\text{Ga}_2\text{S}_5$  powders. Zero field cooled (red) and 500 Oe Field cooled (black) data sets were collected using a 500 Oe measurement field. Inset shows the Curie-Weiss fitting of the high temperature data. (c-d) Magnetization versus applied field for  $\text{Mn}_2\text{In}_2\text{Se}_5$  and  $\text{Mn}_2\text{Ga}_2\text{S}_5$ , respectively, collected at 2K. AC Susceptibility of (e)  $\text{Mn}_2\text{In}_2\text{Se}_5$  and (f)  $\text{Mn}_2\text{Ga}_2\text{S}_5$ . Parameterization of the glassiness behaviour upon fitting the change in the freezing temperature to the Vogel-Fulcher law for (g)  $\text{Mn}_2\text{In}_2\text{Se}_5$  and (h)  $\text{Mn}_2\text{Ga}_2\text{S}_5$ .

The nature of this spin freezing transition can be characterized by calculating the Mydosh parameter<sup>56</sup>,  $\Delta T_f / (T_f * \log(\Delta\omega))$ , with  $T_f$  being the freezing temperature and  $\omega$  the frequency of the AC field. This parameter was calculated for these materials and yielded values of 0.0066 and 0.0085 for  $\text{Mn}_2\text{In}_2\text{Se}_5$  and  $\text{Mn}_2\text{Ga}_2\text{S}_5$ , similar to canonical spin glasses<sup>56-59</sup>, and over an order of magnitude away from Mydosh values indicative of superparamagnetism ( $>0.1$ ).  $T_f$  and  $f$  are related experimentally

by the Vogel-Fulcher-Tammann relation that describes the viscosity of supercooled liquids:  $T_f = T_0 - \frac{E_a}{k_b \ln(\tau_0 * f)}$ , where  $T_0$  is the ideal glass temperature,  $E_a$  is the activation energy of melting, and  $\tau_0$  is the relaxation time. Due to the limited number of data points all three parameters could not be fitted independently and  $\tau_0$  was set to a standard value of  $1 * 10^{-11} \text{ s}$ <sup>48, 60, 61</sup>. Using this  $\tau_0$ , the Vogel-Fulcher-Tammann relation is plotted as an Arrhenius plot in Figure 5 g and h. The extracted  $T_0$  and  $E_a$  for  $\text{Mn}_2\text{In}_2\text{Se}_5$  are 4.3 K and  $1.5 * 10^{-3} \text{ eV}$  and 11.2 K and  $3.2 * 10^{-3} \text{ eV}$  for  $\text{Mn}_2\text{Ga}_2\text{S}_5$ . These are comparable to the previous values reported for  $\text{Mn}_2\text{Ga}_2\text{S}_5$ <sup>48</sup>. The smaller activation energy and  $T_0$  temperature for  $\text{Mn}_2\text{In}_2\text{Se}_5$  indicates an overall smaller interaction strength between the various local magnetic domains across the spin glass transition, likely caused by the Mn/In site disorder in this compound.

### Origin of Magnetic Frustration

Spin glasses are often observed in materials with high amounts of site disorder, or geometric frustration of the magnetic coupling. The origin of the spin glassy behavior seen in these materials cannot be explained solely by site disorder as no site disorder is observed in the crystal structure solution of  $\text{Mn}_2\text{Ga}_2\text{S}_5$ . The source of the magnetic frustration in both materials must be predominantly geometric frustration given the triangular lattice of the Mn atoms. Furthermore, since both materials have appreciable optical band gaps, the electrons must be localized on the Mn atoms and not itinerant, indicating that the magnetic coupling is best described using the Goodenough-Kanamori rules<sup>62, 63</sup>. Looking first at the coupling within just one of the  $\text{MnCh}_6$  octahedral slabs that comprise the double-octahedral thick layers, there are two plausible coupling pathways, as shown in Figure 6 a-c. The first pathway is through the six nearest neighbor  $90^\circ$  Mn-Ch-Mn superexchange pathways which will result in a weakly ferromagnetic coupling interaction that is not frustrated (Figure 6a, b). The second pathway is the direct exchange through nearest neighbor Mn d-orbitals (Figure 6c) and this should lead to antiferromagnetic interactions, that are also relatively weak considering the long Mn-Mn distances in these compounds. Furthermore, direct exchange will result in appreciable geometric frustration, considering the triangular lattice. Together, these two couplings should result in either a low temperature ferromagnetic state or a frustrated antiferromagnetic system and this is what has been reported for these compounds (Table S8).

The addition of the second  $\text{MnCh}_6$  octahedral slab in the  $\text{Mn}_2\text{Tr}_2\text{Ch}_5$  compounds leads to two additional magnetic couplings from the interactions between Mn atoms in neighboring slabs. (Figure 6 d-i). First, there are three  $180^\circ$  superexchange couplings of Mn-Ch-Mn between neighboring layers which should be strongly antiferromagnetic and no frustration. These  $180^\circ$  couplings form 4 separate interpenetrating networks of puckered  $\text{Mn}_6\text{Ch}_6$  honeycombs (Figure 6 f, g). Each Mn atom also has six  $90^\circ$  superexchange coupling pathways between Mn atoms in the other slab, which result in a weakly ferromagnetic inter-slab interaction. Thus, the combination of intra-slab ferromagnetic and antiferromagnetic

superexchange interactions, combined with the inter-slab ferro and antiferromagnetic interactions leads to a high degree of magnetic frustration, and ultimately glassy behavior. It is important to point out that the large magnetic frustration with very low transition temperatures, and spin glass behavior that occurs in these  $\text{Mn}_2\text{Tr}_2\text{Ch}_5$  is very different than what is seen in  $\text{Fe}_2\text{Ga}_2\text{S}_5$ , which is comprised of high-spin  $d^6$   $\text{Fe}^{2+}$  on a nearly identical lattice. However,  $\text{Fe}_2\text{Ga}_2\text{S}_5$  has a very narrow band gap of 5 meV<sup>42</sup>, based on electronic transport measurements. Thus, the itinerant nature of the d-electrons in this case will have very different magnetic coupling interactions, which is apparent considering  $\text{Fe}_2\text{Ga}_2\text{S}_5$  is an antiferromagnet with  $T_N = 110$  K<sup>44</sup>.

$\text{Mn}_2\text{In}_2\text{Se}_5$  and  $\text{Mn}_2\text{Ga}_2\text{S}_5$  have been grown phase pure and can be readily grown in both powder and single crystal forms. The structure and purity of these materials have been shown both through macroscopic X-ray techniques as well as through atomic scale imaging showing long range homogeneity. We have shown these materials to be spin glasses with high levels of magnetic frustration and indirect semiconductors with gaps of 1.33 eV and 1.58 eV for  $\text{Mn}_2\text{In}_2\text{Se}_5$  and  $\text{Mn}_2\text{Ga}_2\text{S}_5$ . The Raman spectra have been fully elucidated as structural signatures and the symmetry of all vibrational modes are identified. The synthesis and characterization of these novel 2D magnetic materials allow for a greater understanding of the fundamentals of 2D material design.

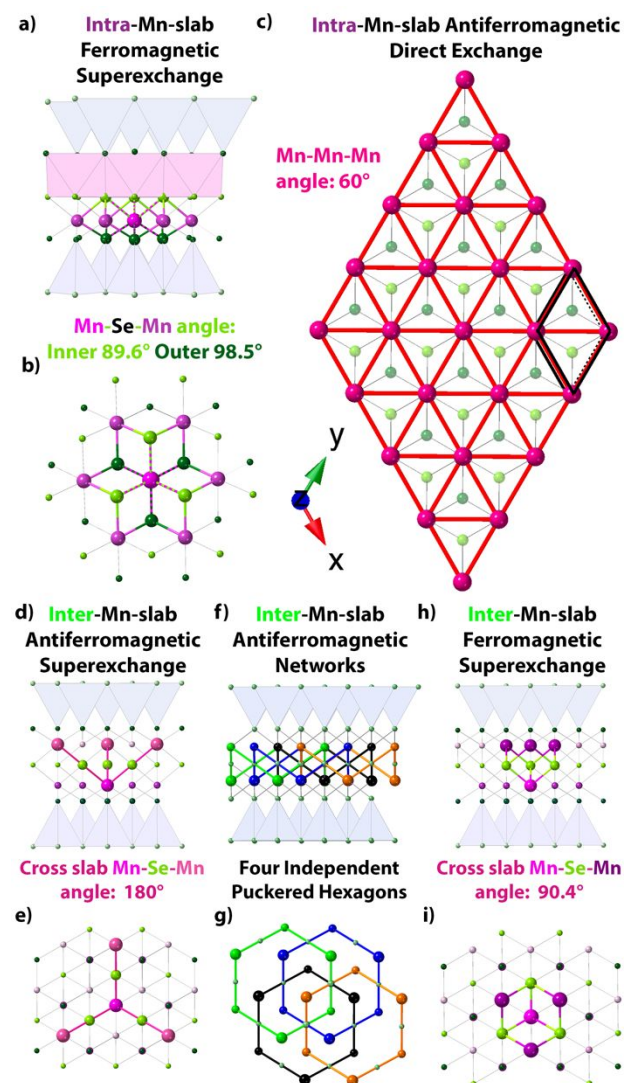


**Fig. 6.** Proposed magnetic coupling pathways in  $\text{Mn}_2\text{In}_2\text{Se}_5$ . Intra-slab  $90^\circ$  ferromagnetic superexchange as viewed a) in-plane and b) cross-plane. c) Intra-slab antiferromagnetic direct exchange as viewed in plane. Inter-slab  $180^\circ$  antiferromagnetic superexchange as viewed d) in-plane and e) cross-plane. Four interlocking networks of antiferromagnetic superexchange pathways as viewed f) in-plane and g) cross-plane with each colour representing a different network. Inter-slab  $90^\circ$  ferromagnetic superexchange as viewed h) in-plane and i) cross-plane.

## Conclusions

## Conflicts of interest

There are no conflicts to declare.

## Acknowledgements

The research of the Goldberger and McComb groups was supported by the Center for Emergent Materials, an NSF MRSEC, under award number DMR-2011876. Electron microscopy was performed at the Center for Electron Microscopy and Analysis (CEMAS) at The Ohio State University. The work within the Windl group was funded by AFOSR project # FA9550-21-1-0268. Computations were performed on the machines of the Ohio Supercomputer Center under project no. PAS0072. We acknowledge support of the Air Force Office of Scientific Research (AFOSR) Grant No. LRIR 23RXCOR003 and AOARD MOST Grant No. F4GGA21207H002 as well as general support from the Air Force Materials and Manufacturing (RX) and Aerospace Systems (RQ) Directorates.

## Notes and references

1. B. Huang, G. Clark, E. Navarro-Moratalla, D. R. Klein, R. Cheng, K. L. Seyler, D. Zhong, E. Schmidgall, M. A. McGuire, D. H. Cobden, W. Yao, D. Xiao, P. Jarillo-Herrero and X. Xu, *Nature (London, U. K.)*, 2017, **546**, 270-273.
2. A. J. Williams and J. E. Goldberger, in *Comprehensive Inorganic Chemistry III (Third Edition)*, eds. J. Reedijk and K. R. Poeppelmeier, Elsevier, Oxford, 3rd edn., 2023, pp. 449-498.
3. R. Bistritzer and A. H. MacDonald, *Proc. Natl. Acad. Sci. U. S. A.*, 2011, **108**, 12233-12237.
4. Z. Jin, Z. Ji, Y. Zhong, Y. Jin, X. Hu, X. Zhang, L. Zhu, X. Huang, T. Li, X. Cai and L. Zhou, *ACS Nano*, 2022, **16**, 7572-7579.
5. S. Kezilebieke, V. Vaňo, M. N. Huda, M. Aapro, S. C. Ganguli, P. Liljeroth and J. L. Lado, *Nano Lett.*, 2022, **22**, 328-333.
6. E. F. Talantsev, R. C. Mataira and W. P. Crump, *Sci. Rep.*, 2020, **10**, 212.
7. T. Song, Q.-C. Sun, E. Anderson, C. Wang, J. Qian, T. Taniguchi, K. Watanabe, M. A. McGuire, R. Stöhr, D. Xiao, T. Cao, J. Wrachtrup and X. Xu, *Science*, 2021, **374**, 1140-1144.

8. H. Xie, X. Luo, Z. Ye, Z. Sun, G. Ye, S. H. Sung, H. Ge, S. Yan, Y. Fu, S. Tian, H. Lei, K. Sun, R. Hovden, R. He and L. Zhao, *Nat. Phys.*, 2023.
9. S. Bruzzone, D. Logoteta, G. Fiori and G. Iannaccone, *Sci. Rep.*, 2015, **5**, 14519.
10. S. Gupta, A. Kutana and B. I. Yakobson, *Nat. Commun.*, 2020, **11**, 2989.
11. J. I. A. Li, T. Taniguchi, K. Watanabe, J. Hone and C. R. Dean, *Nat. Phys.*, 2017, **13**, 751-755.
12. Z. Yan, R. Zhang, X. Dong, S. Qi and X. Xu, *Phys. Chem. Chem. Phys.*, 2020, **22**, 14773-14780.
13. Z.-Z. Lin and X. Chen, *Adv. Electron. Mater.*, 2020, **6**, 1900968.
14. L. Zhang, T. Li, J. Li, Y. Jiang, J. Yuan and H. Li, *J. Phys. Chem. C*, 2020, **124**, 27429-27435.
15. K. Dolui, M. D. Petrović, K. Zollner, P. Plecháč, J. Fabian and B. K. Nikolić, *Nano Lett.*, 2020, **20**, 2288-2295.
16. M. Abramchuk, S. Jaszewski, K. R. Metz, G. B. Osterhoudt, Y. Wang, K. S. Burch and F. Tafti, *Adv. Mater.*, 2018, **30**, 1801325.
17. M. A. McGuire, *Crystals*, 2017, **7**, 121.
18. M. A. McGuire, H. Dixit, V. R. Cooper and B. C. Sales, *Chem. Mater.*, 2015, **27**, 612-620.
19. X. Cai, T. Song, N. P. Wilson, G. Clark, M. He, X. Zhang, T. Taniguchi, K. Watanabe, W. Yao, D. Xiao, M. A. McGuire, D. H. Cobden and X. Xu, *Nano Lett.*, 2019, **19**, 3993-3998.
20. W. L. B. Huey, A. M. Ochs, A. J. Williams, Y. Zhang, S. Kraguljac, Z. Deng, C. E. Moore, W. Windl, C. N. Lau and J. E. Goldberger, *ACS Nano*, 2022, **16**, 3852-3860.
21. Q. Li, X. Zhao, L. Deng, Z. Shi, S. Liu, Q. Wei, L. Zhang, Y. Cheng, L. Zhang, H. Lu, W. Gao, W. Huang, C.-W. Qiu, G. Xiang, S. J. Pennycook, Q. Xiong, K. P. Loh and B. Peng, *ACS Nano*, 2020, **14**, 4636-4645.
22. L. M. Martinez, J. A. Delgado, C. L. Saiz, A. Cosio, Y. Wu, D. Villagrán, K. Gandha, C. Karthik, I. C. Nlebedim and S. R. Singamaneni, *J. Appl. Phys. (Melville, NY, U. S.)*, 2018, **124**, 153903.
23. Y. T. H. Pham, M. Liu, V. O. Jimenez, Z. Yu, V. Kalappattil, F. Zhang, K. Wang, T. Williams, M. Terrones and M.-H. Phan, *Adv. Mater.*, 2020, **32**, 2003607.
24. X. Ding, X. Cui, A. Sohail, P. P. Murmu, J. Kennedy, N. Bao, J. Ding, R. Liu, M. Peng, L. Wang, X. Chu, A. Vinu, S. P. Ringer and J. Yi, *Adv. Quantum Technol.*, 2021, **4**, 2000093.
25. K. Zhang, S. Feng, J. Wang, A. Azcatl, N. Lu, R. Addou, N. Wang, C. Zhou, J. Lerach, V. Bojan, M. J. Kim, L.-Q. Chen, R. M. Wallace, M. Terrones, J. Zhu and J. A. Robinson, *Nano Lett.*, 2015, **15**, 6586-6591.
26. F. Moro, S. Ke, A. G. del Águila, A. Söll, Z. Sofer, Q. Wu, M. Yue, L. Li, X. Liu and M. Fanciulli, *Adv. Funct. Mater.*, 2022, **32**, 2207044.
27. K. Lee, A. H. Dismukes, E. J. Telford, R. A. Wiscons, J. Wang, X. Xu, C. Nuckolls, C. R. Dean, X. Roy and X. Zhu, *Nano Lett.*, 2021, **21**, 3511-3517.
28. E. J. Telford, A. H. Dismukes, K. Lee, M. Cheng, A. Wieteska, A. K. Bartholomew, Y.-S. Chen, X. Xu, A. N. Pasupathy, X. Zhu, C. R. Dean and X. Roy, *Adv. Mater.*, 2020, **32**, 2003240.
29. K. Kim, S. Y. Lim, J. Kim, J.-U. Lee, S. Lee, P. Kim, K. Park, S. Son, C.-H. Park, J.-G. Park and H. Cheong, *2D Mater.*, 2019, **6**, 041001.
30. G. Long, H. Henck, M. Gibertini, D. Dumcenco, Z. Wang, T. Taniguchi, K. Watanabe, E. Giannini and A. F. Morpurgo, *Nano Lett.*, 2020, **20**, 2452-2459.
31. S. Siebeneichler, K. V. Dorn, A. Ovchinnikov, W. Papawassiliou, I. da Silva, V. Smetana, A. J. Pell and A.-V. Mudring, *Chem. Mater.*, 2022, **34**, 7982-7994.
32. F. Islam, T. V. Trevisan, T. Heitmann, S. Pakhira, S. X. M. Riberolles, N. S. Sangeetha, D. C. Johnston, P. P. Orth and D. Vaknin, *Phys. Rev. B*, 2023, **107**, 054425.
33. L. D. Sanjeewa, J. Xing, K. M. Taddei and A. S. Sefat, *J. Solid State Chem.*, 2022, **308**, 122917.
34. S. Zhao, P. D. de Réotier, A. Yaouanc, D. E. MacLaughlin, J. M. Mackie, O. O. Bernal, Y. Nambu, T. Higo and S. Nakatsuji, *Phys. Rev. B: Condens. Matter Mater. Phys.*, 2012, **86**, 064435.
35. M. Kang, S. Fang, L. Ye, H. C. Po, J. Denlinger, C. Jozwiak, A. Bostwick, E. Rotenberg, E. Kaxiras, J. G. Checkelsky and R. Comin, *Nat. Commun.*, 2020, **11**, 4004.
36. K. Zhao, H. Deng, H. Chen, K. A. Ross, V. Petříček, G. Günther, M. Russina, V. Hutanu and P. Gegenwart, *Science*, 2020, **367**, 1218-1223.
37. J. Ji, M. Sun, Y. Cai, Y. Wang, Y. Sun, W. Ren, Z. Zhang, F. Jin and Q. Zhang, *Chin. Phys. Lett.*, 2021, **38**, 047502.
38. A. Banerjee, P. Lampen-Kelley, J. Knolle, C. Balz, A. A. Aczel, B. Winn, Y. Liu, D. Pajerowski, J. Yan, C. A. Bridges, A. T. Savici, B. C. Chakoumakos, M. D. Lumsden, D. A. Tennant, R. Moessner, D. G. Mandrus and S. E. Nagler, *npj Quantum Mater.*, 2018, **3**, 8.
39. J. A. Wilson and A. D. Yoffe, *Adv. Phys.*, 1969, **18**, 193-335.
40. H. Haeuseler and S. K. Srivastava, *Z. Kristallogr. - Cryst. Mater.*, 2000, **215**, 205-221.
41. H. Haeuseler, W. Cordes, D. Reinen and U. Kesper, *J. Solid State Chem.*, 1993, **106**, 501-505.
42. T. Tomita, Y. Nambu, S. Nakatsuji, S. Koeda, M. Hedo and Y. Uwatoko, *J. Phys. Soc. Jpn.*, 2009, **78**, 094603.
43. J. Choi, S. Choi, J. Choi, Y. H. Hwang, Y. H. Um, C. Hong, S. Cho, H.-W. Lee and B.-S. Kim, *J. Korean Phys. Soc.*, 2004, **45**, 672.
44. S. Nakatsuji, H. Tonomura, K. Onuma, Y. Nambu, O. Sakai, Y. Maeno, R. T. Macaluso and J. Y. Chan, *Phys. Rev. Lett.*, 2007, **99**, 157203.
45. K.-J. Range, U. Klement, G. Doll, E. Bucher and J. R. Baumann, *Acta Crystallogr., Sect. C: Cryst. Struct. Commun.*, 1992, **48**, 355-356.
46. C. Cedeño, G. Díaz de Delgado, J. M. Delgado, L. M. de Chalbaud and V. Sagredo, *J. Phys. Chem. Solids*, 2005, **66**, 2049-2051.
47. M.-P. Pardo, P.-H. Fourcroy and J. Flahaut, *Mater. Res. Bull.*, 1975, **10**, 665-675.
48. J. Shen, X. Xu, M. He, Y. Liu, Y. Han and Z. Qu, *Chin. Phys. B*, 2022, **31**, 067105.
49. D. Alfè, *Comput. Phys. Commun.*, 2009, **180**, 2622-2633.
50. G. Kresse and J. Furthmüller, *Phys. Rev. B*, 1996, **54**, 11169-11186.
51. P. E. Blöchl, *Phys. Rev. B*, 1994, **50**, 17953-17979.
52. M. Methfessel and A. T. Paxton, *Phys. Rev. B*, 1989, **40**, 3616-3621.
53. S. L. Dudarev, G. A. Botton, S. Y. Savrasov, C. J. Humphreys and A. P. Sutton, *Phys. Rev. B*, 1998, **57**, 1505-1509.
54. S. Grimme, *J. Comput. Chem.*, 2006, **27**, 1787-1799.
55. S. Cortijo-Campos, P. Kung, C. Prieto and A. de Andrés, *J. Phys. Chem. C*, 2021, **125**, 23904-23910.
56. J. A. Mydosh, *Spin glasses : an experimental introduction*, Taylor & Francis London, London, 1993.

## ARTICLE

## Journal Name

57. F. W. Smith and J. C. Liu, *Solid State Commun.*, 1978, **26**, 91-94.
58. F. W. Smith, *Phys. Rev. B*, 1976, **14**, 241-243.
59. F. S. Liu, W. A. Roshen and J. Ruvalds, *Phys. Rev. B*, 1987, **36**, 492-500.
60. J. W. Krizan and R. J. Cava, *Phys. Rev. B*, 2014, **89**, 214401.
61. Y. Yeshurun, J. L. Tholence, J. K. Kjems and B. Wanklyn, *J. Phys. C: Solid State Phys.*, 1985, **18**, L483.
62. J. Kanamori, *J. Phys. Chem. Solids*, 1959, **10**, 87-98.
63. J. B. Goodenough, *Physical Review*, 1955, **100**, 564-573.